COMPUTER-AIDED CIVIL AND INFRASTRUCTURE ENGINEERING

Computer-Aided Civil and Infrastructure Engineering **33** (2018) 602–613

INDUSTRIAL APPLICATION

Sewer Discharge Estimation by Stereoscopic Imaging and Synchronized Frame Processing

Ekaterina Sirazitdinova, Igor Pesic, Patrick Schwehn & Hyuk Song

Department of Medical Informatics, Uniklinik RWTH Aachen, Aachen, Germany

Matthias Satzger & Marcus Sattler

Seba Hydrometrie, Kaufbeuren, Germany

Dorothea Weingärtner

Research Institute for Water and Waste Management, RWTH Aachen University, Aachen, Germany

&

Thomas M. Deserno*

Peter L. Reichertz Institute for Medical Informatics, University of Braunschweig, Braunschweig, Germany

Abstract: *A system for fully automatic contact-less image-based measurement of volumetric flow rate in urban drainage structures is presented. The hardware includes two original equipment manufacturer cameras and a single-board computer on which our custom image processing software is running. The value of water discharge depends on the surface velocity, water level and channel's geometry. The level of the flow is estimated as the difference between distances from the camera to the water surface and from the camera to the channel's bottom. Camera-to-water distance is recovered automatically using large-scale stereo-matching, whereas the distance to the channel's bottom is measured upon installation. Surface velocity is calculated using cross-correlation template matching: individual natural particles in the flow are detected and tracked throughout the sequence of images recorded over a fixed time interval. The relative discharge computation error is lower than 1.34% of the theoretical maximal discharge for a given location, which makes our system competitive to commercial components such as ultrasonic flow meters, while using cheaper technologies.*

*To whom correspondence should be addressed. E-mail: *Thomas.deserno@plri.de*.

DOI: 10.1111/mice.12365

1 INTRODUCTION

Blockages or breakages of sewer lines, inflows of excessive storm water, malfunction of pumping stations or electrical power failures may lead to sewer overflows (SOs). Upon the occurrence of such events, waste water is discharged from a sewer into nearby streams, rivers, or other water bodies prior to reaching treatment facilities. SOs pose a huge risk to the environment, as they contain industrial waste, toxic materials, and debris. Reaching water bodies, pollutants threaten public health, endanger aquatic life, and impair the use and enjoyment of waterways (Wilkinson et al., 2002; Burkhardt et al., 2007; Rodríguez et al., 2012). To avoid this problem, constant monitoring and quantitative and qualitative measurements of water flow in sewers is required.

Besides prevention of SOs, discharge monitoring is used to control pump stations and service pits. To

reduce the cost of transporting wastewater from the user to the treatment plant, such pump stations are built to lift the wastewater to a higher level. Then, gravity is used to enable a natural flow of wastewater towards the treatment plant. Thus, by knowing the sewage level, the operating efficiency of the sewage system can be enhanced.

Monitoring of sewer flows is challenging. Most of the state-of-the-art systems for volumetric flow measurement, such as the positive displacement flow meter require intrusion into the flow (Spitzer, 2005). Taking into account the demolishing nature of waste water, such systems are usually short-lived in a real sewer environment and require regular maintenance. Moreover, such equipment usually is expensive, and, thus, its usage is limited.

There are also noninvasive methods. One of them is ultrasonic flow meter (Lynnworth, 1989). It measures the level in a channel by transmitting a pulse of sound from the sensor to the flow surface and estimating the time for the echo to return. However, this method is not robust against presence of foam, turbulence, floating debris, oil, or grease. Furthermore, it is not recommended to use this method on wide channels due to beam spread.

In two complementary works, Nguyen et al. (2009) and Jeanbourquin et al. (2011) proposed an alternative nonintrusive solution. The authors of both papers have jointly developed a system tracking volumetric flows in sewers using video cameras. According to the authors, the video camera setup is robust against instrumental loss and does not require frequent maintenance. Volumetric flow rate is measured by combining image-based approaches of water-level measurement and surface velocity estimation. Despite relatively high accuracy of water-level estimation claimed by the authors (the root mean square [RMS] error varied between 1.33 and 4.61 cm compared to the ground truth for different observations), there is a major inconvenience in the proposed technique relying on the detection of water borderline in the images: the described scenario requires calibration relative to the real-world coordinates. For that, special rulers are placed into the scene, and experts manually choose correspondences. This complicates the initial setup in the field and originates additional sources of error. Furthermore, no evaluation was done in terms of real-world velocities and no result of pure image-based volumetric flow estimation was presented.

Aiming at providing an automatic, robust, and noncontact flow measurement in urban drainage structures, we came up with an original idea of a vision-based system. Introducing a second camera to the setup (Müller and Deserno, 2015), we exploit stereo-vision techniques to recover water level in sewers and to achieve automatic calibration to the real-world coordinates. Accompanied with a velocity estimation module, our system is able to provide accurate measurements of water discharge in sewers of known geometry.

2 OVERVIEW

2.1 Determination of water discharge

In sewers, discharge is computed using a simplified form of the continuity equation. According to this method, flow discharge Q, $[Q] = \text{m}^3/\text{s}$, is determined by the relationship between average flow velocity $\bar{v}$, $[\bar{v}] = \text{m/s}$, and the cross-sectional area $A(l)$, $[A(l)] = \text{m}^2$, of the channel perpendicular to the predominant flow direction (Herschy, 1998)

$$Q = \bar{v}\, A\,(l)$$

In the sewer with a uniform geometry (constant slope and profile), the value of $A(l)$ depends on the current water level l, $[l] = \text{m}$, and the geometry of the channel. In the system for discharge assessment, all parameters necessary for the computation of A except for l can be given upon installation (Section 3). Thus, the basic milestones of the automatic volumetric flow computation are finding the water level l and the velocity $\bar{v}$.

2.2 Water-level estimation

The most common image-based method estimating the water level in sewers and other water bodies (e.g., rivers, open channels) is the optical interpretation of special rulers (Nguyen et al., 2009; Gilmore et al., 2013; Bruinink et al., 2015) or detection of reference indicators (Kim et al., 2007), which require a ruler or a special pattern placed into the scene. Alternatively, we introduce a second camera to the setup for automatic level estimation, which does not require any extrinsic objects. Reconstructing the scene in 3D, we are able to recover the distance l_{surface} from the camera to the water surface. The water level l is then estimated as a difference between the distance from the camera to the channel's bottom l_{total} and l_{surface}.

2.3 Velocity measurement

Image-based methods of flow measurement are often based on detection and tracking of artificial (Weitbrecht et al., 2003; Aleixo et al., 2011; Tauro et al., 2013) or natural (Jeanbourquin et al., 2011) particles. Similarly to Jeanbourquin et al. (2011), we rely on the presence

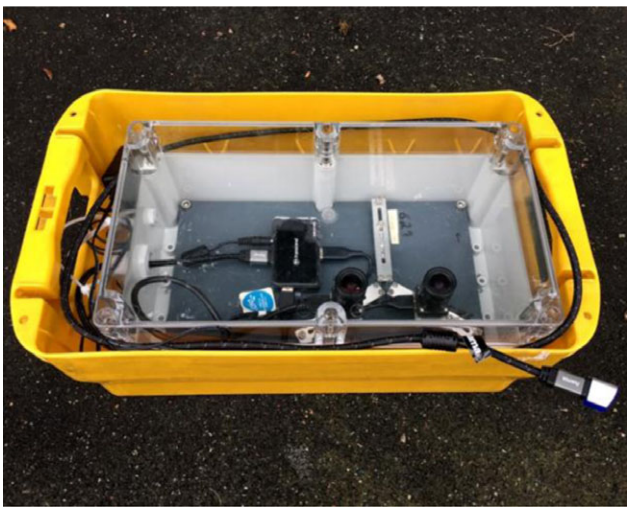

Fig. 1. Sensors.

Fig. 2. Placement of the recording hardware into an open channel.

of natural particles in the sewers. We use template matching (Lewis, 1995) to find displacements between particles in sequential frames. Individual velocities v of particles are found by division of these displacements by the value of the known time interval between the frames.

Furthermore, exploiting the advantage of having two cameras, we apply triangulation (Hartley and Sturm, 1997) to recover z-coordinates, or depth values, of individual particles. This is useful for identification of particles on the surface and supports water-level estimation.

3 SYSTEM DESIGN

The life cycle of our system can be divided into three major stages: (i) manufacturing, (ii) installation at the user's location, and (iii) exploitation. System components used at each of these stages are sensors, or cameras, processing units, and storage hardware.

In particular, the recording hardware consists of a lighting element and two original equipment manufacturer (OEM) cameras (Figure 1). Except for assembling the hardware components during *manufacturing*, a camera calibration (Section 4.1) shall be done for each new system to correct for lens distortion and to determine the relation between the camera's natural units (pixels) and the real-world units (mm). These calibration parameters are saved together with system settings into an XML file and delivered together with the client software to the final user.

Installation at user's location includes placement of the recording device into the sewer (Figure 2), measurement of the location-specific values such as channel's geometry and distance from the installed camera to the channel's bottom, selection of preliminary region of interest (ROI) and insertion of all numerical data into browser-based client software. Due to the fact that sewer profiles are usually conventional, being of a circular, ovoid, arch, walkway, or rectangular shape with standardized measurements, this task can be reduced to the selection of the corresponding profile in the user settings. Custom profiles are also supported. In that case, all necessary parameters shall be measured and recorded into the system. Measurement of such parameters and the distance from the camera to the channel's bottom is a crucial step, because erroneous value will directly affect the system's outcome. In cases with the profile shapes different from rectangular, by distance to the bottom we understand the length of the orthogonal interval from the deepest channel point to the camera plane. The selected location-specific settings are transferred to the operational web-server saving the data on the storage device.

During *exploitation*, images are recorded within scheduled intervals and temporarily stored on a single-board computer (SBC), also known as communication circuit board (TQMLS102xA board: http://www.tq-group.com/), where they are being processed by a custom image processing software implemented in C++. The general algorithmic pipeline of discharge computation involves two major steps: depth reconstruction and surface velocity computation (Figure 3). All supportive steps are described in detail in the next section. Outcomes of the image processing are transferred to the user and stored in the storage. The session images are moved from the SBC to the storage and can be accessed by the user upon request.

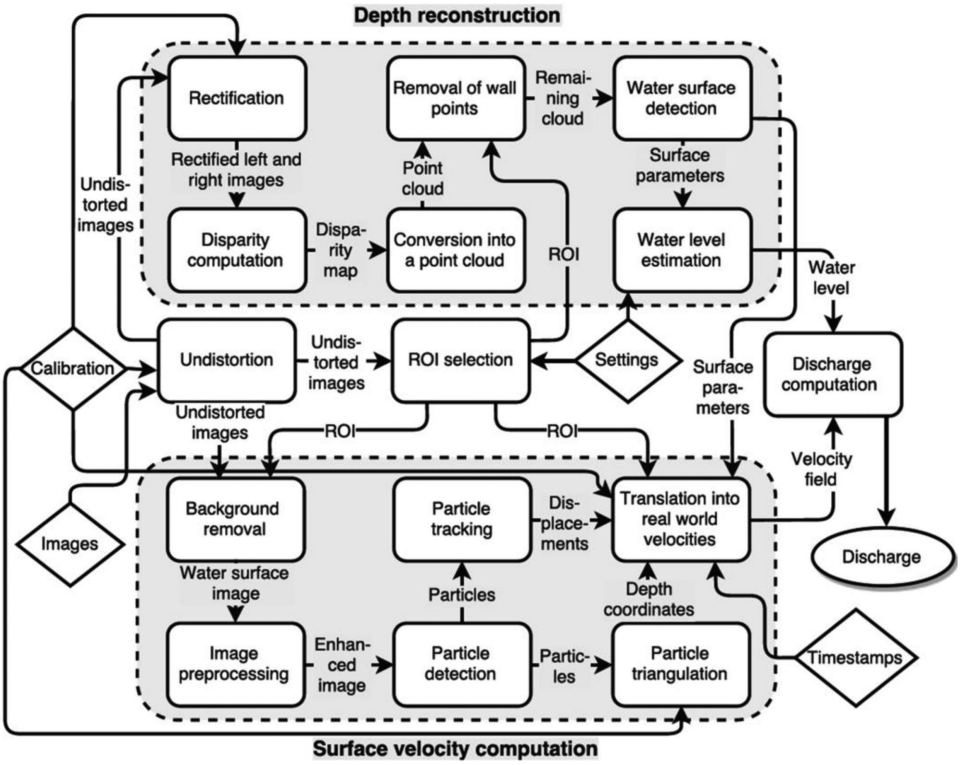

Fig. 3. General algorithmic pipeline.

4 IMAGE PROCESSING SOFTWARE

4.1 Camera calibration

Camera calibration is needed to obtain accurate depth estimation and image processing results, as well as to produce a reference value for conversion between the image and the world coordinate systems. With a chessboard calibration protocol, the intrinsic and extrinsic parameters are estimated for each camera (Zhang, 2000).

Using intrinsic parameters, we correct the original 2D images for distortion effects caused by imperfections of the optical system. If not treated, these effects would certainly lower the accuracy of depth and surface velocity measurements. In order to get an undistorted image, each pixel in the original image is mapped to its correct position using the Brown–Conrady distortion model, which adds a tangential component to the radial distortion (Brown, 1966).

The extrinsic parameters define the position of the camera center and the camera's orientation in world coordinates. Using extrinsic parameters, we can estimate the distance between two cameras in real-world units, which is used for conversion from image coordinates to real-world units (Section 4.2).

4.2 Water-level estimation

4.2.1 General water level. The water level l is estimated as a difference between distances from the camera setup to the water surface and to the channel's bottom. The latter is measured once upon installation. The distance to the water surface is computed using large-scale stereo-matching (Geiger et al., 2011). This method computes disparity maps from rectified grayscale stereo-pairs by performing a triangulation on a set of support points that can be robustly matched. This method does not require global optimization, and, therefore, is fast.

The process runs as follows: (i) the images are undistorted and rectified (Section 4.1); (ii) image contrast is equalized by applying contrast limited adaptive histogram equalization (CLAHE) (Zuiderveld, 1994); (iii) a dense disparity map is calculated for the given image pair, where one image pair represents two images recorded simultaneously with the right and the left cameras (Geiger et al., 2011); (iv) using intrinsic camera parameters, the disparity map is reprojected to a point cloud with 3D coordinates (X, Y, Z) in the world coordinate space; (v) the points within the ROI that belong to the channel's walls and surrounding areas are removed from the model—the remaining points either belong to the water surface, or can be classified as

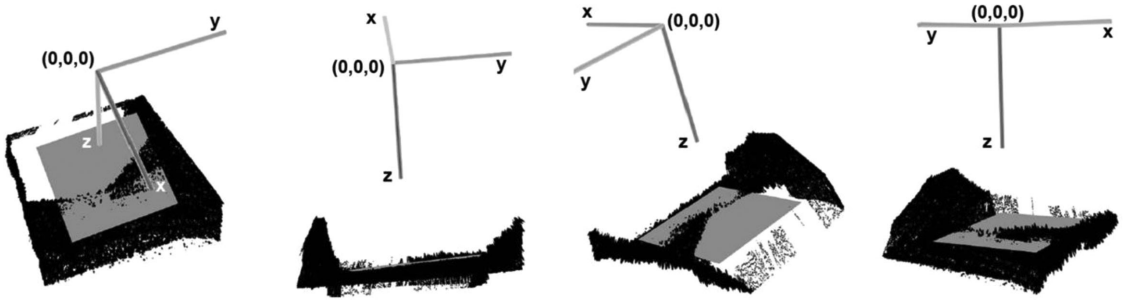

Fig. 4. Water surface detected in the reconstructed point cloud shown from different perspectives. The point cloud scene including water surface and channel walls is depicted in black. The gray square is a parametric plane fitted into the water surface. The coordinate system is placed to origin; camera direction corresponds to the z-axis.

outliers caused by water reflections or resulting from the reprojection error; and (vi) the parametric water surface plane $D = K\ X + L\ Y + M\ Z$ is approximated using the maximum likelihood estimation sample consensus (MLESAC) algorithm (Torr and Zisserman, 2000). The approximated plane should be parallel to the image plane with allowed offset of 5° (Figure 4).

For robust estimation of the distance to the water surface, we compute disparity maps for several left-right pairs of images. We set the number of pairs to 20, but it may vary depending on the allowed computational time: the more pairs are taken, the more robust is the result. After running all these steps for each image pair, we calculate the trim mean of the water surface plane as an average of values between 20th and 80th quantiles of all values of plane models resulting in a single plane equation $D' = K'\ X + L'\ Y + M'\ Z$. The distance l_{surface} from the camera to the water surface is then computed as

$$l_{\text{surface}} = \frac{\left|K'X_0 + L'\ Y_0 + M'Z_0 + D'\right|}{\sqrt{K'2 + L'2 + M'2}}$$

where (X_0, Y_0, Z_0) are the coordinates of the origin.

4.2.2 Z-coordinate estimation. Computing individual z-coordinates of particles is beneficial for velocity estimation (particles which lie below the surface can be removed) and for the robustness of depth estimation (the estimated depth value l_{surface} shall be approximately the same as the z-value of the majority of particles in the flow).

To compute individual z-coordinates, images from both cameras are exploited. Correspondences between particles in a left-right pair are established using fast normalized cross-correlation (Lewis, 1995), similarly to the particle tracking. The disparities of the matched particles are computed using linear least-squares triangulation (Hartley and Sturm, 1997). Conveniently, this not only allows detection of z-coordinates, but also the computation of x- and y-coordinates of a particle in the real-world coordinate system.

If enough natural particles can be robustly detected in the flow (at least two particles per frame visible by both of the cameras), the final depth value can be derived from individual z-values as a statistical mode of the whole set of values in the image sequence. For the scenes lacking natural particles, general depth level can be still computed using large-scale stereo-matching.

4.3 Velocity measurement

The velocity of the flow is estimated by tracking particles of interest in the sequential frames. These can be small pieces of floating waste highly distinguishable from the background water. The processing pipeline is composed of (i) image preparation, (ii) detection of natural particles, (iii) tracking of detected particles in sequential frames, (iv) removal of outliers, and (v) estimation of velocity values using displacement vectors and timestamps.

4.3.1 Image preparation. Images coming directly from the cameras often feature some undesired artifacts such as wavy light reflections, traces of rain or condensate, and shadows. When untreated, they undermine particle tracking by creating false matches or outliers, or leaving some important particles undetected. We apply a simple image processing pipeline: (i) the images are cropped to the selected ROI for a more robust particle tracking; (ii) CLAHE is applied for image equalization (Figure 5a); (iii) gradient edge detection is applied to transform the image into an edge image; (iv) the detected edges are emphasized by grayscale dilation with a circle-shaped kernel (Figure 5b); (v) the image is binarized with a simple threshold: we set up the threshold value to 4% of maximum intensity in the image (Figure 5c); (vi) all remaining objects in the scene are presented as connected components; (vii) the connected

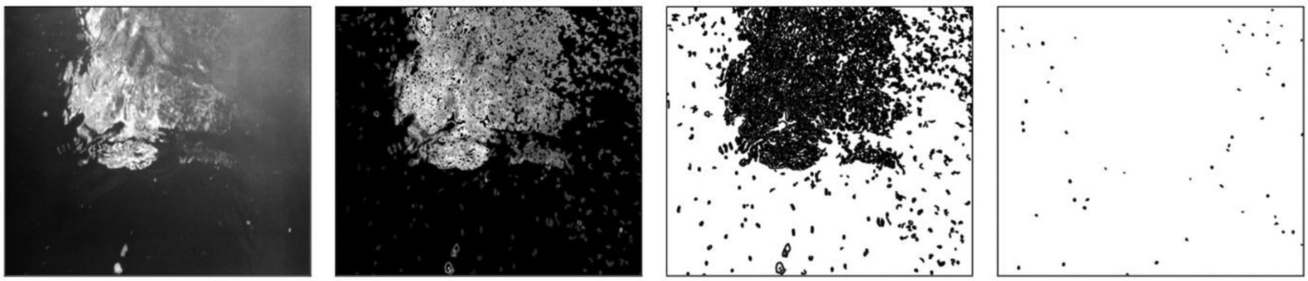

Fig. 5. Image preprocessing for particle detection: (a) original image cropped to the ROI equalized with CLAHE filter; (b) dilated edge image; (c) binarized image (inverted for a better visibility); and (d) remaining particles after reflection removal.

components are then classified as reflections and other objects based on their length: reflections, normally having a larger size (we set the threshold to 40 pixels, which is equivalent to 1.2 cm^2), are eliminated (Figure 5d); and (viii) morphological erosion is applied to the remaining objects to set their size back to the original.

4.3.2 Particles detection. In the binarized images, particles are located using simple blob detection based on the connected-component labeling (Suzuki and Abe, 1985). We label a detected blob as a particle if it has more than three pixels. Large objects are represented as groups of particles.

4.3.3 Particles tracking. In order to find the correspondences between the particles in sequential images, template matching is used: a function slides through the image and compares the overlapped windows of size $w \times h$ (w — window's width, h — window's height) against the input image using fast normalized cross-correlation (Lewis, 1995). For more effective computations the searched area is narrowed down to a certain size (we take an area limited by a circle with a radius of 40 pixels, which is 8.3% of image height, with a center in the particle coordinates). Probabilities of different possible matches are estimated, the window with higher matching probability is localized and the particle correspondences are established. Matches of probability lower than 30% are discarded. The parameter values were derived empirically as a trade-off for minimizing outliers while maintaining a sufficient number of found matches.

The detection of particle correspondences is a crucial step for discharge computation. The method still works even if there are just few correspondences, however, in such a situation, the final result might be affected by outliers, and, therefore, the system is considered to be more robust in the scenarios when a bigger number of particles and particle correspondences can be detected. Because only few correspondences between particles are normally detected in pairs of sequential images (Figure 6a), we benefit from processing the whole image sequence and combining all detected correspondences together in a vector field, which is shown to be sufficient for a robust velocity computation (Figure 6b).

4.3.4 Removal of outliers. Because template matching may identify false correspondences between particles, an outlier removal algorithm was developed. Considering drag forces and presence of turbulence, surface velocities are usually inconsistent and angles of movement may vary depending on the particle position. Therefore, we split the ROI into a grid of cells and detect local outliers in each cell.

The cells containing a small number of vectors are ignored. If the vector field contains m vectors in n cells, the threshold for a sufficient number of vectors in a cell will be $0.1\frac{m}{n}$. The local outliers are identified using the iterative random sample consensus (RANSAC) algorithm (Fischler and Bolles, 1981): at each iteration (the total number is 50), one vector from the cell $\widehat{ij}$ is selected as a reference vector and compared with each other vector $\widehat{i'j'}$ in the same cell. The score τ of the reference vector is

$$\tau = \sum_{\forall \widehat{i'j'}} \left[\|\widehat{ij} - \widehat{i'j'}\| < 0.2 \, \|\widehat{ij}\| \right]$$

The reference vector with the highest score is selected as representative for the cell velocity, and all others highly deviating from this vector are classified as outliers and removed.

4.3.5 From displacements to surface velocities. So far, particle displacements are considered in terms of image coordinates (pixels). To translate the calculated values into the real-world units (mm), the pixel-to-millimeter ratio r is computed for each displacement vector individually by division of the distance in pixels between

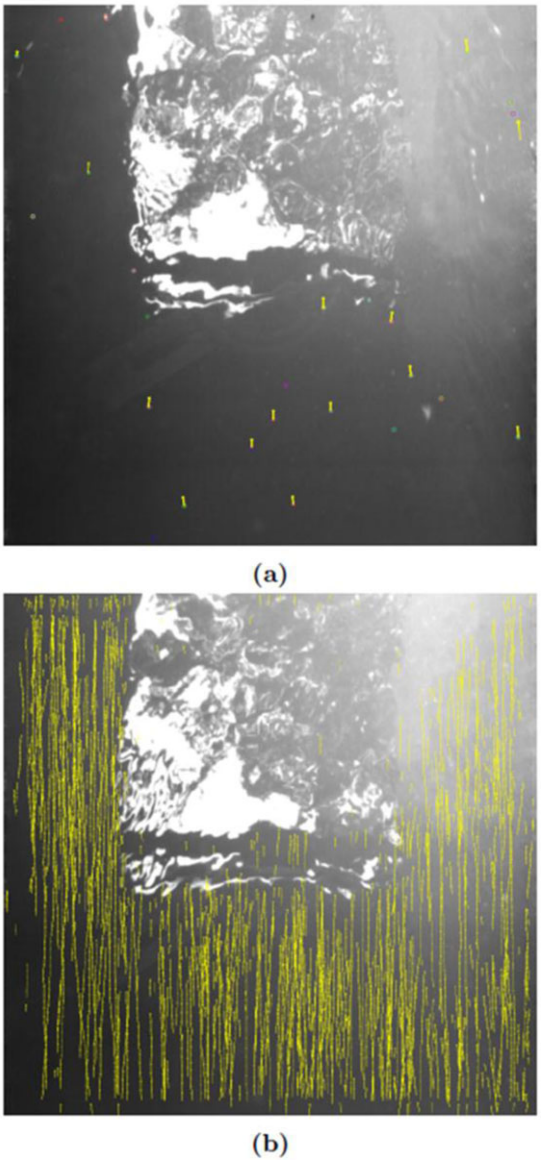

Fig. 6. Particle tracking: (a) found correspondences between the particles in two sequential images and (b) the vector field over the whole sequence of images.

two original points (i.e., those on the image plane) by the real distance between the corresponding particles.

We propose two methods for estimation of the real distances. The first method relies on particle triangulation. For each displacement vector with known real-world coordinates of its starting point, we apply triangulation to find the real-world coordinates of its ending point. The real-world distance is then estimated as a Euclidean norm of the displacement vector in real-world coordinates. Assuming that the scaling factor in the rectified image shall be the same for each displacement vector, we derive a general ratio as a statistical mode of all individual ratios in the image sequence. This general ratio is applied to each displacement vector including those for which estimation of real-world coordinates was not possible.

The second approach is designed for the image sequences lacking natural particles. It employs the approximated water surface plane. We select two points (starting and ending points of displacement vector) in the image and project them on the water surface plane extending the ray from the principal point of the camera through the point on the image plane all the way to the water surface. The reprojected points are used for the estimation of the distance in real-world units.

To calculate the velocity, we are using individual timestamps indicating exactly when each image pair was recorded. Thus, the time interval is measured for each image pair individually, and the velocity v of each vector is derived by dividing the displacement value in mm by the value of time shift in seconds.

4.4 Extra functionality

4.4.1 Automatic ROI detection. To resolve the ambiguity of water surface detection for water-level estimation (Section 4.2) and to minimize the chances of false points being classified as particles of interest for tracking (Section 4.3), it is necessary to localize the ROI enclosing the flow surface only.

In most of the usage scenarios, the camera is placed perpendicularly to the channel so that two borders of the channel are present in the scene. In this case, ROI is detected automatically as an area limited by the left and right channel borders, which are detected using the generalized Hough transform (Ballard, 1987). Alternatively, the ROI can be selected manually by the user upon installation.

4.4.2 Extraneous object detection. A frequent reason of sewer malfunction is a presence of extraneous objects or clogs in the channel. Our algorithm supports detection of such objects. For that, we have extended our pipeline (Section 4.3): we compare the values of representative displacements in each grid cell with each other. The cells with a representative vector considerably different from the common flow are labeled as suspected to contain extraneous objects or clogs. Common flow vector is also computed using RANSAC, and the deviation from the common flow is indicated by comparison $\|\widehat{ij} - \widehat{i'j'}\| > 0.8\|\widehat{ij}\|$, where, in this case, $\widehat{ij}$ is used for the common flow vector and $\widehat{i'j'}$ for each representative vector in a cell. Of course, this can work only if an undesired object is located within the viewing range of the cameras.

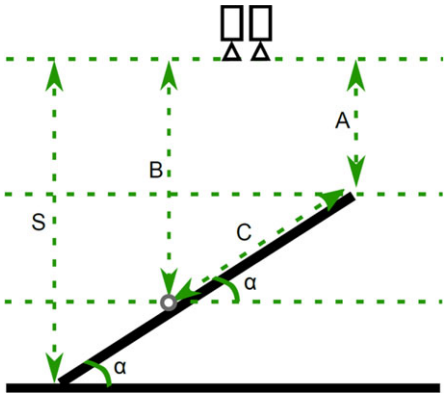

Fig. 7. *Z*-coordinate experimental setup. The board with artificial particles is placed at a certain angle to the bottom, which provides that all particles lie at different distances from the camera setup.

5 EXPERIMENTS AND RESULTS

5.1 *Z*-coordinate experiment

In order to assess the quality of estimation of individual z-coordinates of particles, an artificial setup was prepared.

5.1.1 Data set. We placed 16 artificial particles (white circles) of different sizes on a black mat board. The board was installed so that one of its edges was touching the bottom and the other one was fixed so that the board's lateral projection would form an angle α with the bottom (Figure 7). The camera setup was placed parallel to the bottom over the board and a single stereo-image pair was recorded. Then we changed the angle α and rotated the camera setup by 90°. Another image pair was recorded.

For each of the two installations, we measured the angle α (37° and 18°), the distance A from the cameras' plane to the upper edge of the border (69.3 cm and 84.8 cm), and the distance S from the cameras' plane to the bottom (101.3 cm in both cases). Additionally, for each of the artificial particles, the distance C from the particle to the border's upper edge was measured.

5.1.2 Method. Automatic z-coordinate detection was applied on both pairs of images, and, for each artificial particle, the distances B' to the cameras' plane were recovered. The absolute error of our method was assessed computing the difference between distance B' and the corresponding theoretical distance B from the cameras' plane to the particle

$$B = A + C \sin \frac{\pi \alpha}{180}$$

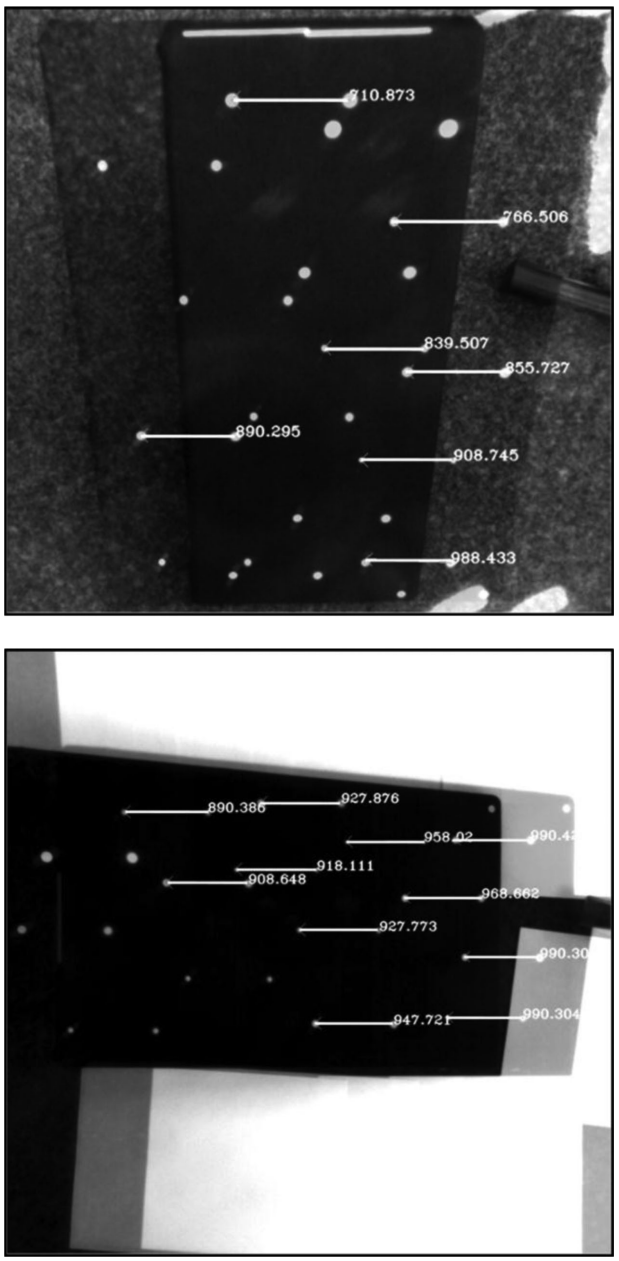

Fig. 8. Automatically generated z-test results' close-ups of two experiments: images are rectified and overlaid and the correspondences between matched particles are shown together with the recovered z-values.

The relative error was estimated as a ratio of RMS error computed on absolute errors and the measuring range (the distance S).

5.1.3 Result. In the first image pair (Figure 8, top), we were able to estimate z-coordinates of seven artificial particles. The RMS error was 0.51 cm, which is 0.51% of the measuring range. In the second image pair (Figure 8,

bottom), depth value of 11 particles was recovered, and the RMS error was 0.55 cm, or 0.54% of the measuring range.

5.2 *In situ* validation

The preliminary evaluation in real conditions (Sirazitdinova et al., 2017) has shown that our system performs similarly to the one of Nguyen et al. (2009) and Jeanbourquin et al. (2011), which to our knowledge was the only development in the field so far. However, due to the experimental design, the acquired result was only a rough estimate, which could be used as a proof of concept only. In order to assess the real performance of our system, a new experiment was designed and performed.

5.2.1 Data set. Two data sets were recorded in two different sewage treatment plants. Both of them have open segments of rectangular shape where we installed our recording device (Figure 2). In both locations, we recorded several image sequences: each 8 seconds long with a varying frame rate (20–30 fps). Depending on the frame rate, each sequence consists of 160–240 stereo-image pairs. In the beginning of each session, a reference depth value l_{ref} was measured with a rigid ruler and the reference value of volumetric flow Q_{ref} was recorded.

The *Stolberg* data set consists of 13 image sequences. The channel in the spot of measurement is relatively wide (140 cm), the discharge on the day of measurement was moderate (176–236 l/s). The reference value of discharge was measured with a combination of a venturi and an ultrasonic flow meter. The distance from the camera to the channel's bottom was 210.5 cm.

The *PIA* data set consists of 12 sequences. Comparing to the first location, the channel here is rather narrow (25 cm), with the rather stable discharge of 3.6–4.06 l/s. We covered the open segment to model low-light environment. The HydroRanger ultrasonic-level controller (Siemens, Germany) was used to record the reference values.

5.2.2 Method. For each image sequence, the following values were computed automatically using the developed image processing software:

- Average velocity $\bar{v}$,
- Distance from the sensor to the water surface l_{surface}.

In the rectangular profile, knowing the width of the channel w_{channel} and the total distance from the sensor to the channel's bottom l_{total}, and having automatically estimated the velocity $\overline{v}$ and the distance from the sensor to the water surface l_{surface}, the volumetric flow Q was estimated as

$$Q = \overline{v}\ w_{\text{channel}}\ (l_{\text{total}} - l_{\text{surface}})$$

Reference values for surface velocity were not available. However, it was possible to compute theoretical surface velocity $\overline{v}_{\text{theor}}$ from the reference volumetric flow Q_{ref} and depth l_{ref}

$$\overline{v}_{\text{theor}} = \frac{Q_{\text{ref}}}{w_{\text{channel}}\ l_{\text{ref}}}$$

The absolute water-level error δ_l was computed as a difference between the estimated depth $(l_{\text{total}} - l_{\text{surface}})$ and reference value l_{ref}. The absolute surface velocity error δ was computed as a difference between $\overline{v}_{\text{theor}}$ and $\overline{v}$. The absolute discharge error δ_Q was calculated as a difference between Q and Q_{ref}.

The relative water-level error values ε_l were computed as ratios of absolute error values δ_l and the values of the measuring ranges (which is in that case the distances from the camera to the channel's bottom l_{total}). The relative surface velocity errors ε_v were computed as ratios of absolute error values δ_v and the theoretical surface velocity maximum $v_{\max}$ for given locations. In order to calculate $v_{\max}$, we divided the theoretical maximal discharge $Q_{\max}$ computed using the Colebrook–White equation (Colebrook, 1939) by the value of maximal possible sewer cross-section area $A_{\max}$ computed using known sewer width and height (in case of rectangular profile). The relative discharge errors ε_Q were calculated as ratios of δ_Q and $Q_{\max}$.

5.2.3 Result. In both cases, the experimentally determined values of water level, surface velocity and discharge resulted close by the reference values obtained from ultrasonic flow meters. For the two data sets, the RMS errors of water-level estimation were 1.1 cm and 0.8 cm (0.52% and 0.67%) in case of z-based estimation, and 6.5 cm and 3.1 cm (3.08% and 2.55%) for stereo-measurement based on the large-scale stereo-matching without particles (Tables 1 and 2). The RMS errors of surface velocity estimation were 3.2 cm/s and 0.8 cm/s (2.15% and 0.67%). The RMS errors of discharge computation were 12.2 l/s and 1.34 l/s (0.29% and 1.34%). Comparing the relative RMS error values, we observe that the water-level estimation based on z-coordinates is rather precise. The deviation of surface velocities is slightly incremented.

6 DISCUSSION

Comprehensive evaluation included depth measurement in an artificial setting, a series of preliminary

Table 1
Absolute errors δ_l, δ_v, and δ_Q

	Stolberg data set				*PIA data set*			
	Water level δ_l (z-based), cm	*Water level δ_l (stereo), cm*	*Velocity δ_v, cm/s*	*Discharge δ_Q, l/s*	*Water level δ_l (z-based), cm*	*Water level δ_l (stereo), cm*	*Velocity δ_v, cm/s*	*Discharge δ_Q, l/s*
Min error	0.1	0.3	0.1	0.04	0.3	0.08	0.1	0.04
Max error	1.9	16.2	8.7	27.93	1.6	6.1	5.9	1.41
Average error	0.9	5.1	2.3	8.41	0.7	2.3	2.3	0.57
RMS error	1.1	6.5	3.2	12.2	0.8	3.1	2.7	0.67

Table 2
Relative errors $\boldsymbol{\varepsilon}_l$, $\boldsymbol{\varepsilon}_v$, and $\boldsymbol{\varepsilon}_Q$ in %

	Stolberg data set				*PIA data set*			
	Water level ε_l (z-based)	*Water level ε_l (stereo)*	*Velocity ε_v*	*Discharge ε_Q*	*Water level ε_l (z-based)*	*Water level ε_l (stereo)*	*Velocity ε_v*	*Discharge ε_Q*
Min error	0.05	0.14	0.04	0.0	0.25	0.07	0.16	0.08
Max error	0.9	7.7	5.82	0.67	1.33	5.13	11.62	2.79
Average error	0.43	2.44	1.54	0.2	0.6	1.93	4.48	1.14
RMS error	0.52	3.08	2.15	0.29	0.67	2.55	5.38	1.34

experiments in real conditions, and two final recording sessions in different locations. Considering both experiments, in artificial and real environments, we achieved an accurate water-level estimation with a slightly enlarged error of surface velocity estimation, which is explained by the fact, that velocity estimation depends on depth estimation, and, thus, the error gets accumulated. However, the discharge measure is not affected notably and plausable results are still obtained.

The depth measurement based on z-coordinate estimation using triangulation is more accurate than based on large-scale stereo-matching. However, with RMS errors of 3.1–6.5 cm (2.55–3.08%), which is still a good estimate, it can be used as a backup solution for temporary situations, where natural particles are unavailable. In particular, it improves the approaches of Nguyen et al. (2009) and Jeanbourquin et al. (2011), resulting in smaller RMS errors (0.52–1.1 cm vs. 1.33–4.61 cm for depth estimation in real conditions) and provides improved functionality (fully automatic calibration without the need of additional rulers and the possibility of measurements, even if the water–wall borderline is not in the scene). Our system is also competitive with state-of-the-art solutions (ultrasonic flow meters), using at the same time cheaper technologies and yielding discharge estimation errors about 1.34% with the respect to the theoretical maximal discharge for a given location. The total cost of our prototype is approximately US$7,300, but its mass production (20 units and more) would allow a market price of about US$3,000.

The processing time varied between 30 and 150 seconds depending on the number of images and the number of detected particles in a single image: the more particles the longer the computation but the more robust the results. Some operations can be computed in parallel but the current hardware does not support parallel computing. Currently, the processing time is sufficient for frequent measures. As the framerate does not impact the accuracy, the computational load can be reduced if required.

Our experiments have shown that the system operates with different weather conditions in open as well as closed environments, but not with strong rain or stormy winds in open environments. When the water surface turns rough, neither the particle detection nor the parametric surface fitting is accomplished successfully. In previous works (Sirazitdinova et al., 2017) we recorded data in open environment with moderate raindrops, and the system has been proven to be sufficiently robust. If the system is mounted within a manhole (closed environment), only condensate may occasionally drop down to the water surface. The artificial light source proved to be sufficient for particle detection and tracking. Nevertheless, strong rain indeed has an impact

to our system: in combined sewers, the flow intensity is changed when rain mixes with wastewater. On the other hand, more natural particles are available in the flow, and the particle tracking becomes even more robust.

In the next iteration, we are planning a series of experiments to evaluate the impact of several parameters on the system's performance, such as the minimal required number of detected particles, frame rate, and recording length. The current setting of parameters yields sufficient performance. Reducing the frame rate or recording time will enable faster and, hence, more frequent computations. Further evaluation will also include different light and weather conditions, in different times of a day and also in locations with different sewer cross-sections. We believe that adaptive parameters will support the different use case scenarios.

Additionally, our future tasks include hardware reliability and usability tests with prospective end users. We plan to investigate how often hardware maintenance (cleaning of the protective glass and battery replacement) will be required. For that, a prototype will be placed into a chosen location and its long-term performance will be observed. Another option would be shifting computational load from the circuit board to the server, which would allow parallel computations and processing of larger data. However, that would also require reliable transport of big amounts of data from the sensors to the server. Often, network connections in sewer environments are unstable. Therefore, data processing in place (as it is done now) might be the better option. We aim at investigating this issue in the future, too.

7 CONCLUSION

In this work, a novel vision-based solution for automatic contact-less measurement of water discharge has been proposed. Our system automatically computes discharge in sewers and open channels with low light conditions. The proposed method does not require artificial tracking markers, fully relying on the presence of natural particles in waste water. Furthermore, the water-level measurement is possible without any particle.

The described system is a fully functioning prototype. Besides the image processing software, the tool for manufacturing and the client module are also implemented. The manufacturing tool is used for the initial camera calibration. In the client software, location-specific settings can be chosen and the measured values can be received and displayed to the user.

We believe that due to its compactness, usage of relatively cheap technologies, maintainability and portability, our system has a big potential in waste water monitoring and SOs prevention. Furthermore, we also believe that such a vision-based monitoring system, with some adaptation, might be useful for prediction of floods in natural water bodies, or as a survey mechanism for industrial discharge monitoring to provide plant operators with control information.

ACKNOWLEDGMENTS

This work has been funded and supported by German Federation of Industrial Research Associations (AiF), cooperation project 3285001WM4. We want to thank J. Schunicht and B. Böttcher for recording the data.

REFERENCES

Aleixo, R., Soares-Frazão, S. & Zech, Y. (2011), Velocity-field measurements in a dam-break flow using a PTV Voronoï imaging technique, *Experiments in Fluids*, **50**(6), 1633–49.

Ballard, D. H. (1987), Generalizing the Hough transform to detect arbitrary shapes, in M. A. Fischler and O. Firschein (eds.), *Readings in Computer Vision: Issues, Problems, Principles, and Paradigms*, Morgan Kaufmann Publishers Inc., San Francisco, CA, USA, pp. 714–25.

Brown, D. C. (1966), Decentering distortion of lenses, *Photometric Engineering*, **32**(3), 444–62.

Bruinink, M., Chandarr, A., Rudinac, M., van Overloop, P. J. & Jonker, P. (2015), Portable, automatic water level estimation using mobile phone cameras, in *Proceedings of the 14th IAPR International Conference on Machine Vision Applications*, IEEE, Tokyo, Japan, pp. 426–29.

Burkhardt, M., Kupper, T., Hean, S., Haag, R., Schmid, P., Kohler, M. & Boller, M. (2007), Biocides used in building materials and their leaching behavior to sewer systems, *Water Science & Technology*, **56**(12), 63–67.

Colebrook, C. F. (1939), Turbulent flow in pipes with particular reference to the transition region between the smooth and rough pipe laws, *Journal of the Institution of Civil Engineers*, **11**(4), 133–56.

Fischler, M. A. & Bolles, R. C. (1981), Random sample consensus: a paradigm for model fitting with applications to image analysis and automated cartography, *Communications of the ACM*, **24**(6), 381–96.

Geiger, A., Roser, M. & Urtasun, R. (2011), Efficient large-scale stereo matching, in R. Kimmel, R. Klette, and A. Sugimoto (eds.), in *Proceedings of the 10th Asian Conference on Computer Vision*, Springer-Verlag Berlin Heidelberg, Queenstown, New Zealand, pp. 25–38.

Gilmore, T. E., Birgand, F. & Chapman, K. W. (2013), Source and magnitude of error in an inexpensive image-based water level measurement system, *Journal of Hydrology*, **496**, 178–86.

Hartley, R. I. & Sturm, P. (1997), Triangulation, *Computer Vision and Image Understanding*, **68**(2), 146–57.

Herschy, R. W. (1998), *Encyclopedia of Hydrology and Water Resources*, Springer Netherlands, Dordrecht, Netherlands.

Jeanbourquin, D., Sage, D., Nguyen, L. S., Schaeli, B., Kayal, S., Barry, D. A. & Rossi, L. (2011), Flow measurements in sewers based on image analysis: automatic flow

velocity algorithm, *Water Science & Technology*, **64**(5), 1108–14.

Kim, K., Lee, N.-K., Han, Y. & Hahn, H. (2007), Remote detection and monitoring of a water level using narrow band channel, in *Proceedings of the 6th WSEAS International Conference on Signal Processing, Robotics and Automation*, World Scientific and Engineering Academy and Society, Corfu Island, Greece, pp. 25–30.

Lewis, J. P. (1995), Fast normalized cross-correlation, *Vision Interface*, **10**(1), 120–23.

Lynnworth, L. C. (1989), *Ultrasonic Measurements for Process Control: Theory, Techniques, Applications*, Academic Press, Inc., Orlando, FL, USA.

Müller, K. & Deserno, T. M. (2015), Verfahren Zur Erfassung Des Volumenstroms Einer in Einem Gerinne Fließenden Flüssigkeit Sowie Vorrichtung Zur Durchführung Desselben. German Patent 27286 DE 102011055007.0, filed.

Nguyen, L. S., Schaeli, B., Sage, D., Kayal, S., Jeanbourquin, D., Barry, D. A. & Rossi, L. (2009), Vision-based system for the control and measurement of wastewater flow rate in sewer systems, *Water Science & Technology*, **60**(9), 2281–89.

Rodríguez, R. A., Gundy, P. M., Rijal, G. K. & Gerba, C. P. (2012), The impact of combined sewage overflows on the viral contamination of receiving waters, *Food and Environmental Virology*, **4**(1), 34–40.

Sirazitdinova, E., Pesic, I., Schwehn, P., Song, H., Satzger, M., Weingärtner, D., Sattler, M. & Deserno, T. M. (2017), Stereo vision for fully automatic volumetric flow measurement in urban drainage structures, in *Proceedings of the SPIE 10332, Videometrics, Range Imaging, and Applications XIV*, International Society for Optics and Photonics, Munich, Germany.

Spitzer, D. W. (2005), *Industrial Flow Measurement*, ISA-The Instrumentation, Systems, and Automation Society, Research Triangle Park, NC, USA.

Suzuki, S. & Abe, K. (1985), Topological structural analysis of digitized binary images by border following, *Computer Vision, Graphics, and Image Processing*, **30**(1), 32–46.

Tauro, F., Grimaldi, S., Porfiri, M. & Petroselli, A. (2013), Fluorescent particles for non-intrusive surface flow observations, *Procedia Environmental Sciences*, **19**, 895–903.

Torr, P. H. S. & Zisserman, A. (2000), MLESAC: a new robust estimator with application to estimating image geometry, *Computer Vision and Image Understanding*, **78**(1), 138–56.

Weitbrecht, V., Uijttewaal, W. & Jirka, G. H. (2003), 2-D particle tracking to determine transport characteristics in rivers with dead zones, in *Proceedings of the International Symposium on Shallow Flows*, Delft, the Netherlands, pp. 1–8.

Wilkinson, D. H., Armstrong, D. J. & Blevins, D. W. (2002), *Effects of Wastewater and Combined Sewer Overflows on Water Quality in the Blue River Basin, Kansas City, Missouri and Kansas*, U.S. Dept. of the Interior, Washington DC, USA.

Zhang, Z. (2000), A flexible new technique for camera calibration, *IEEE Transactions on Pattern Analysis and Machine Intelligence*, **22**(11), 1330–34.

Zuiderveld, K. (1994), Contrast limited adaptive histogram equalization, *Graphics Gems IV*, Academic Press Professional, Inc., San Diego, CA, USA, pp. 474–85.